Ultrasonics Sonochemistry 75 (2021) 105585

Contents lists available at ScienceDirect

Ultrasonics Sonochemistry

journal homepage: www.elsevier.com/locate/ultson

Preparation of $MgTi_2O_5$ nanoparticles for sonophotocatalytic degradation of triphenylmethane dyes

Thangavel Selvamani [a], Sambandam Anandan [a,*], Abdullah M. Asiri [b], Pichai Maruthamuthu [c], Muthupandian Ashokkumar [d]

[a] Nanomaterials and Solar Energy Conversion Lab, Department of Chemistry, National Institute of Technology, Tiruchirappalli 620 015, India
[b] The Center of Excellence for Advanced Materials Research, King Abdulaziz University, Jeddah 21413, P.O. Box 80203, Saudi Arabia
[c] Department of Energy, University of Madras, Guindy Campus, Chennai 600025, India
[d] School of Chemistry, University of Melbourne, Vic 3010, Australia

ARTICLE INFO

Keywords:
$MgTi_2O_5$ nanoparticles
Sonocatalytic
Photocatalytic
Sonophotocatalytic activity
Synergetic effect

ABSTRACT

$MgTi_2O_5$ (magnesium dititanate) nanoparticles were prepared by a simple hydrothermal assisted post-annealing method and characterized with various analytical techniques. The catalytic properties (sonocatalytic, photocatalytic and sonophotocatalytic activity) were evaluated using the degradation of triphenylmethane dyes (crystal violet, basic fuchsin, and acid fuchsin). The sonophotocatalytic activity of $MgTi_2O_5$ nanoparticles towards crystal violet was found to be ~2.9 times higher than the photocatalytic activity and ~20 times higher than that of the sonocatalytic processes. In addition, the sonophotocatalytic efficiency of $MgTi_2O_5$ nanoparticles was found to be remarkable for the degradation of basic fuchsin (cationic dye) and acid fuchsin (anionic dye). The mechanism of these catalytic activities has been discussed in detail.

1. Introduction

Magnesium oxide (MgO) with an energy bandgap of >5.4 eV is found to show excellent photocatalytic activity due to the presence of reactive sites (defects or low coordinated sites) on the surface [1–3]. To tune, the energy bandgap of composite materials such as TiO_2/MgO heterostructures and magnesium titanates ($MgTiO_3$, Mg_2TiO_4, and $MgTi_2O_5$) have been developed [4–10]. Among these materials, $MgTi_2O_5$ (magnesium dititanate) has a theoretical energy bandgap of ~3.4 eV with orthorhombic phase and pseudobrookite-type structures [9,10]. The formation of pure $MgTi_2O_5$ phase is found to be difficult due to the formation of mixed phases such as $MgTiO_3$-$MgTi_2O_5$. Hence, recent studies are focus on the controlled growth of the pure $MgTi_2O_5$ phase [10]. $MgTi_2O_5$ has been found useful in several applications such as white pigment, thermistor, water purification, sodium-ion batteries, and photocatalyst for hydrogen production by water splitting [9–15]. Triphenylmethane dyes (methyl violet, crystal violet, malachite green, basic fuchsin, acid fuchsin, and cresol red) are mostly employed in the textile industry for colouring and as a food preservative in seafood industries. The discharge of these dyes into water bodies poses serious harmto human health [16,17]. In the past decades, numerous techniques (adsorption, membrane filtration, coagulation, incineration, and microbial degradation) have been employed for the removal of organic contaminants from wastewater [18,19]. Unfortunately, the conventional processes are ineffective for the removal of pollutants [20,21]. Advanced oxidation processes (AOPs) are used for the mineralization of harmful toxic pollutants present in wastewater. In these processes, highly reactive oxidizing radicals (e.g., $^{\bullet}OH$) are produced that react with organic pollutants and convert them into harmless products [22]. Acoustic cavitation is classified as an AOP since it generates highly reactive oxidizing radicals within cavitation bubbles that have been used in environmental remediation for the degradation of pollutants in aqueous solutions [23–26]. Photocatalysis, Fenton process, ozonation, electro-chemical/catalytic techniques, etc, also generated highly reactive radicals that are used for the degradation of organic pollutants [27–33]. The photocatalytic process involves the use of solar energy to initiate oxidation/reduction reactions over semiconductors. Both sonolysis (acoustic cavitation) and photocatalysis have some disadvantages that could be overcome by combining these techniques. The combined/hybrid technique is known as sonophotocatalysis and has been shown to provide some synergistic advantages compared to individual techniques [24,34–36]. In the current study, we prepared

* Corresponding author.
E-mail address: sanand@nitt.edu (S. Anandan).

https://doi.org/10.1016/j.ultsonch.2021.105585
Received 9 January 2021; Received in revised form 30 April 2021; Accepted 5 May 2021
Available online 7 May 2021

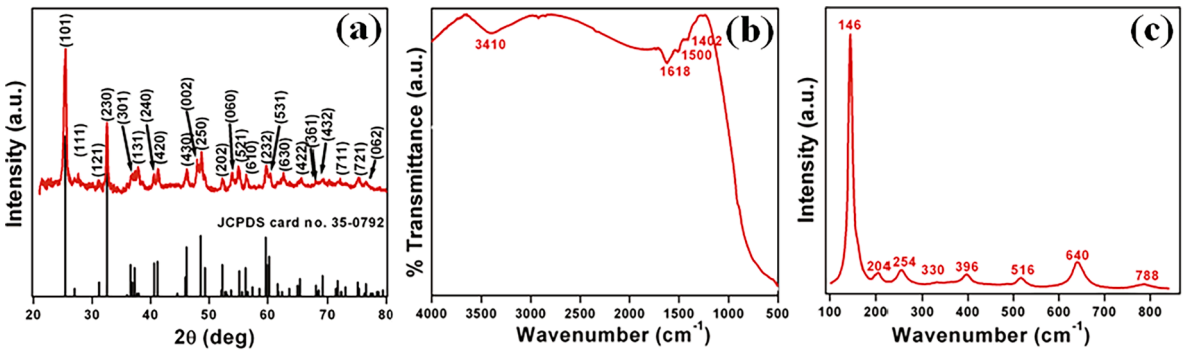

Fig 1. (a) Powder XRD pattern, (b) FTIR spectrum, and (c) Raman spectrum of $MgTi_2O_5$.

$MgTi_2O_5$ nanoparticles by a simple hydrothermal assisted post-annealing method and used them for the degradation of triphenylmethane dyes (crystal violet, basic fuchsin, and acid fuchsin) by sonocatalytic, photocatalytic and sonophotocatalytic processes.

2. Experimental procedure

2.1. Materials

Magnesium(II) nitrate hexahydrate (ACS reagent, 98.0–102.0%), titanium(IV) isopropoxide (99%), urea (ACS reagent, 99.0–100.5%), crystal violet (CV; ACS reagent, ≥99.0%), basic fuchsin (BF; >85%), acid fuchsin (AF; ~70%), nitroblue tetrazolium (NBT; 90.0–11.0%) and terephthalic acid (reagent grade, 98%) were received from Sigma-Aldrich and used without further purification. Ethylene glycol (≥99%) was purchased from Merck

2.2. $MgTi_2O_5$ nanoparticles preparation

About 3.84 g of magnesium (II) nitrate hexahydrate dissolved in 30 mL of aqueous urea solution (~12 g) was added to 40 mL of ethylene glycol containing 6 mL of titanium isopropoxide in a 250 mL round bottom flask. Then, the solution mixtures were kept at 90 °C for 24 h under ambient conditions with constant stirring. Subsequently, the product was collected and washed with distilled water and dried at 110 °C for 4 h. Finally, the calcination of this product was carried out at 600 °C for 2 h produces $MgTi_2O_5$ as nanoparticles.

2.3. $MgTi_2O_5$ nanoparticles characterization

The crystalline structure of the $MgTi_2O_5$ sample was characterized by a powder X-ray diffractometer (XRD) (Rigaku D/max-2500 utilizing Cu Kα radiation). The chemical structure of the sample was analyzed by Fourier transform infrared (FTIR) spectra using Nicolet iS50 infrared spectrophotometer by KBr pellet technique. Raman spectra of the sample were recorded using the EnSpectr RS-532 Raman system. Surface morphology and structural analysis were done by field emission scanning electron microscopy (FESEM model JEOL 7401F) and transmission electron microscopy (TEM model FEI Tecnai F30 microscope operated at 300 kV). The elemental analysis was carried out by an energy-dispersive X-ray spectrometer (EDS, Oxford Inc attached with FESEM). The chemical states of the elements were analyzed by X-ray photoelectron spectroscopy (XPS) (Physical Electronics PHI 5600 spectrophotometer with monochromatic Al Kα (1486.6 eV)). The UV–visible absorption spectrum was measured by an ultraviolet–visible (UV–vis) spectrophotometer (T90+, PG Instruments, UK). The photoluminescence (PL) spectra of the samples were recorded on Shimadzu (RF5301PC) spectrofluorometer. The surface potential (ζ-zeta) was measured by Zetasizer Nano Zs/ZEN3600, Malvern instrument. Herein, the sample (about 1–2 mg in 5 mL) is prepared using deionized water followed by sonication for dispersion. The pH of solutions has been adjusted by using dilute HCl and NaOH.

2.4. Experimental setup and catalytic activity of triphenylmethane dyes degradation

The ultrasonic reactor was operated at 38 kHz frequency and 100 W power (Kaijo 30110, Japan). The reactor was operated in its maximum volume capacity of 1 L. The photocatalytic activity was performed with a 6 W UV lamp (Heber Scientific, India, emitting light radiation of 365 nm as the light source) immersed in quartz well placed at the middle of the reactor [37]. A typical batch photoreactor was used with 100 mL of 5×10^{-5} mol L^{-1} triphenylmethane dyes. About 50 mg of catalyst (0.5 g L^{-1}) was added and stirred for 30 min under dark conditions to attain adsorption/desorption equilibrium between the dye molecules and surface of the catalyst. Following this process, the solution mixture was illuminated with a UV lamp (for the photocatalytic process) or US irradiation (sonocatalytic process) or a combination of both for sono-photocatalytic processes (both UV illumination + US irradiation). At regular time intervals, 4 mL of dye solution was collected and the catalyst was removed by filtration by a PVDF syringe filter (0.45 μm). The degradation efficiencies [(η, %) were calculated using Eq. (1)]

$$\eta = [A_0 - A_t / A_0] \times 100\% \quad (1)$$

where, A_o and A_t are absorbance and concentration of the dye solutions before and after degradation treatment, respectively.

2.5. Generation of superoxide ($O_2^{\bullet -}$) radical species analysis

The quantity of superoxide radical species generated by the sono and photocatalytic processes were measured by UV–vis spectroscopy. For this experiment, about 100 mg of catalyst was taken in 100 mL (conc. 5×10^{-5} mol L^{-1}) of nitroblue tetrazolium solution. Then, the reaction mixture was subjected to the photocatalytic process. At regular time intervals, 4 mL of solution were collected and the catalyst was filtered by PVDF syringe filter (0.45 μm). The absorbance was analyzed by UV–vis spectrophotometer.

2.6. Generation of hydroxyl radical ($^{\bullet}OH$) analysis

The detection of hydroxyl radicals under the sono and photocatalytic processes was carried out by a simple photoluminescence technique. About 100 mg of catalyst was added to 100 mL of terephthalic acid (conc. 5×10^{-4} mol L^{-1}) in a base solution (conc. 2×10^{-3} mol $L^{-1}$of NaOH). The reaction mixture was subjected to the photocatalytic process. At regular time intervals, 4 mL of solutions were collected and the catalyst was filtered by PVDF syringe filter (0.45 μm). Then, the PL measurement was carryout with an excitation wavelength at 315 nm.

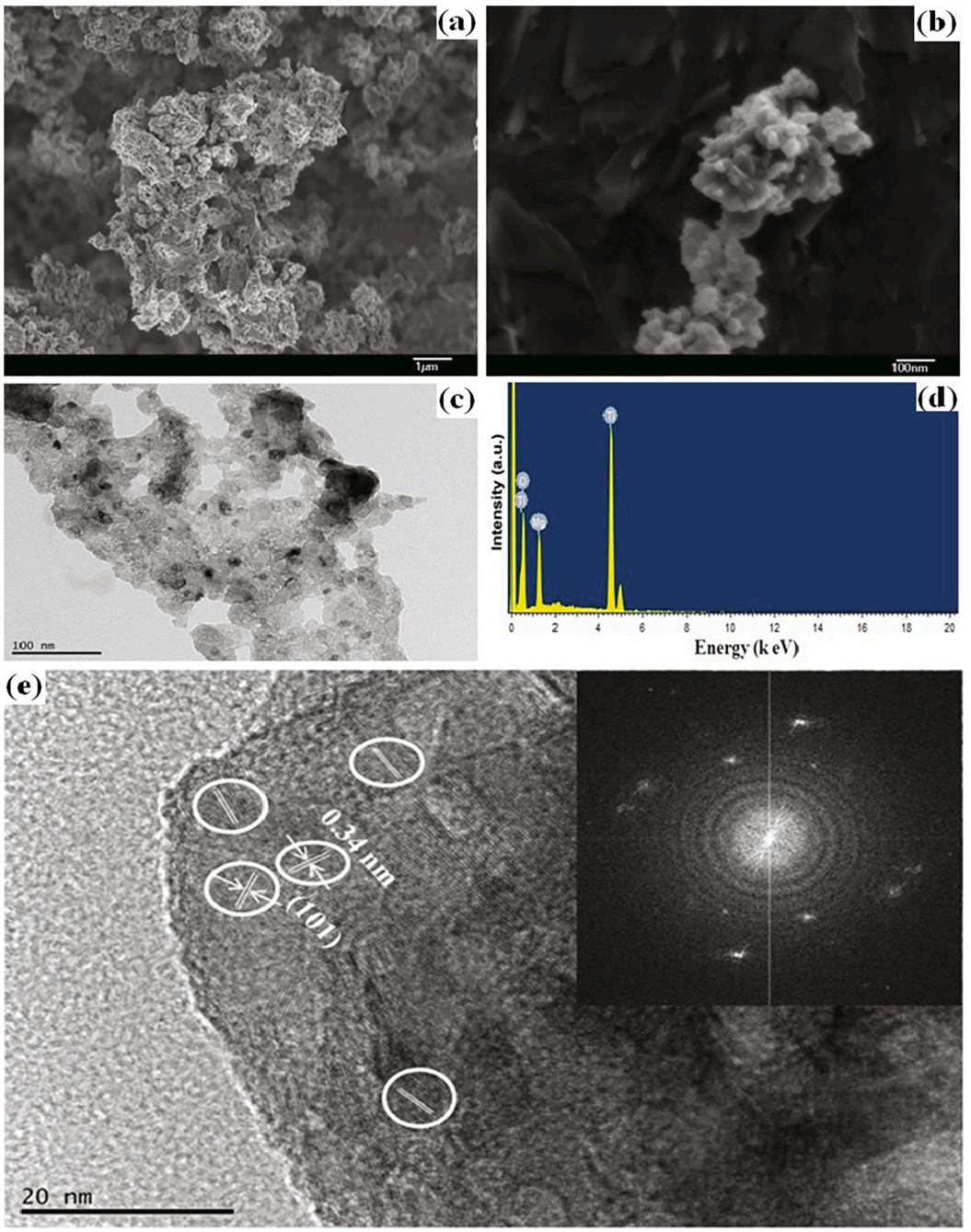

Fig 2. (a-b) FESEM image, (c) TEM image, (d) EDS spectrum and (e) HRTEM image of $MgTi_2O_5$ nanoparticles (inset the corresponding FFT image).

3. Results and discussion

The main aim of this work was to synthesize a highly active photocatalyst $MgTi_2O_5$. In order to confirm the formation of $MgTi_2O_5$ several characterization techniques were used. Fig. 1a shows the powder XRD pattern of the as-prepared catalyst. The diffraction peaks at $2\theta = 25.4°$, 26.9°, 31.2°, 32.5°, 36.5°, 37.2°, 40.6°, 41.2°, 46.1°, 48.5°, 49.3°, 52.2°, 55.1°, 56.2°, 57.3°, 59.6°, 60.2°, 63.1°, 65.4°, 68.0°, 69.1°, 73.0°, 75.1° and 76.5° are indexed to the (101), (111), (121), (230), (301), (131), (240), (420), (430), (002), (250), (202), (060), (521), (610), (232), (531), (630), (422), (361), (432), (711), (721) and (062) planes of orthorhombic phase for the Karroite ($MgTi_2O_5$; JCPDS card no. 35-0792) [10,14]. Further, no other peaks were observed in the XRD spectrum suggesting the formation of the pure phase of $MgTi_2O_5$. The FTIR spectrum of this sample is shown in Fig. 1b. The observed peaks at 3410 cm^{-1} and 1660 cm^{-1} correspond to O–H vibration due to the presence of water (chemisorbed/physisorbed) on the surface. The characteristic peaks at 1500 cm^{-1} and 1402 cm^{-1} can be assigned to surface bicarbonate species [3]. Raman spectrum of the sample is presented in Fig. 1c. The sample exhibits several bands at 146, 204, 254, 330, 396, 516, 640 and 788 cm^{-1} that could be assigned to ν_1, ν_6, ν_7, ν_9, ν_{10}, ν_{14}, ν_{16} and ν_{17} vibration modes (A_g, B_{1g}, B_{1g}, and B_{3g}), respectively [38,39]. Thus, the above results provide support to the formation of $MgTi_2O_5$ with a crystalline orthorhombic phase of Karroite [39].

The morphological features of the as-synthesized $MgTi_2O_5$ sample are shown in Fig. 2a-c. At low magnification, the FESEM image of $MgTi_2O_5$ appears in honeycomb-like structures, consisting of a large number of nanoparticles (Fig. 2a). The higher magnification image shows a clearer image of nanoparticles (Fig. 2b). The TEM image provides additional information on the structure of $MgTi_2O_5$ (Fig. 2c). The

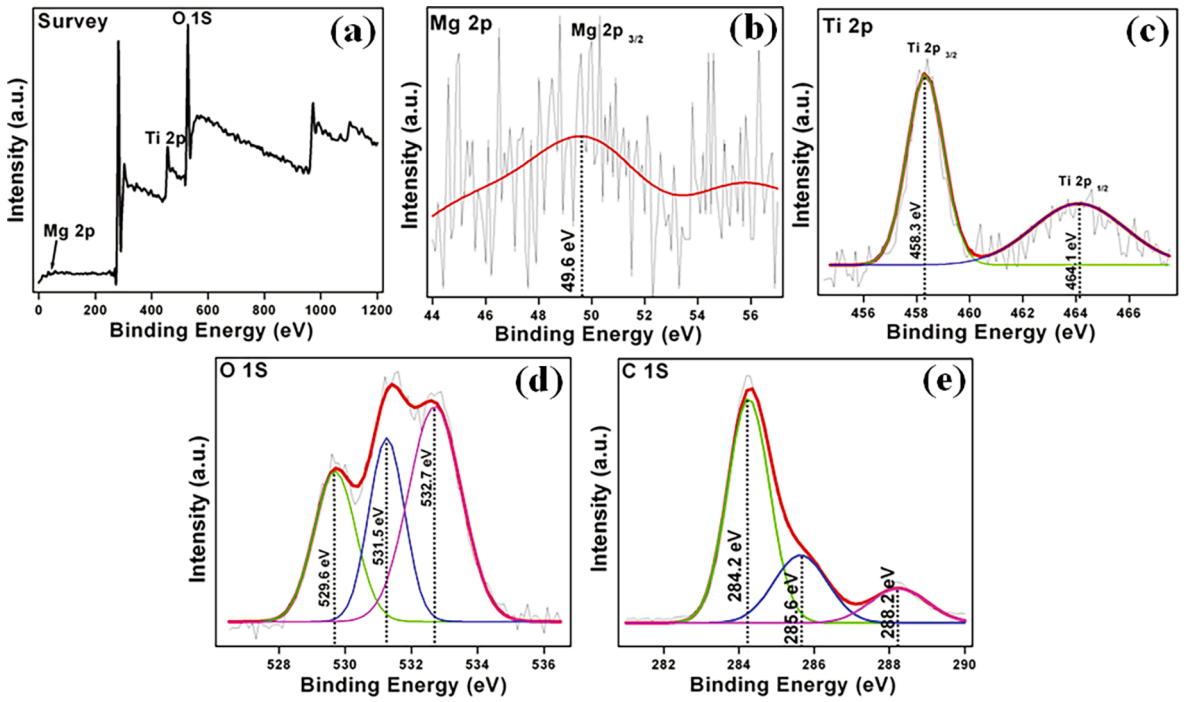

Fig 3. XPS spectrum of $MgTi_2O_5$ nanoparticles (a) survey scan, (b) Mg 2p, (c) Ti 2p, (d) O1s and (e) C1s peaks.

EDS pattern of the $MgTi_2O_5$ sample is shown in Fig. 2d. Herein, the peaks of Mg, Ti, and O elements can be found. The HRTEM image indicates that a lattice fringe of 0.34 nm could be ascribed to the (1 0 1) plane for the orthorhombic phase of $MgTi_2O_5$ (Fig. 2e and inset the corresponding FFT image) [10].

The chemical states and elemental composition of $MgTi_2O_5$ nanoparticles were evaluated by XPS analysis (Fig. 3). As shown in the survey spectrum (Fig. 3a), the presence of Mg, Ti, and O is confirmed and the results are in good agreement with EDS results. Further, in this core-level signal at 49.6 eV for Mg 2p as the strong peak is ascribed to Mg $2p_{3/2}$ (Fig. 3b) and the Ti 2p spectrum displayed into two peaks at 458.3 and 464.1 eV for Ti $2P_{3/2}$ and Ti $2P_{1/2}$, respectively (Fig. 3c). Then, the O 1s spectrum can be fitted into three spectral peaks at 529.6, 531.5, and 532.7 eV due to lattice oxygen, adsorbed oxygen, and hydroxyl oxygen, respectively (Fig. 3d) [40,41]. Besides, surface-coordinated bicarbonate species (hydrocarbon, carbon–oxygen contaminants, and carbonate ion) consist of three peaks at 279.5, 283.4, and 288.7 eV for C 1S present on the $MgTi_2O_5$ nanoparticles [41,42].

To evaluate the catalytic activity of $MgTi_2O_5$ nanoparticles for sonocatalytic, photocatalytic, and sonophotocatalytic degradation of triphenylmethane dyes was performed. Here, the aqueous solution of CV dye showed a strong absorption peak at 591 nm. Further, the temporal evolution of CV degradation for sonocatalytic, photocatalytic and sonophotocatalytic processes showed a decrease in that absorption with reaction time (Fig. 4a-c). However, the absorption peak intensities of sonocatalytic process (only US irradiation) indicate that the slight degradation (relatively lower) when compared with photocatalytic and sonophotocatalytic processes (Fig. 4a). Whereas, in the case of photocatalytic process (only UV illumination), a higher degradation was observed when compared with sonocatalytic and lesser degradation when compared with sonophotocataltic processes (Fig. 4b). Whilst, the sonophotocatalytic process (both US + UV) showed complete degradation of CV at 75 min (Fig. 4c). For comparison, the adsorption (equivalently about ~16%) and degradation profiles for different experiments are presented in Fig. 4d. The result of sonophotocatalytic process shows maximum degradation efficiency (~96%) followed by photocatalytic (72%) and sonocatalytic (28%) at 75 min (Fig. 4d-e). Also, the degradation kinetics is shown by plotting -ln(C/C_0) against irradiation time (Fig. 4f). The observed pseudo-first-order degradation rate constants (k) are found to be 0.0402 min^{-1} (sonophotocatalytic), 0.0142 min^{-1} (photocatalytic), and 0.00197 min^{-1} (sonocatalytic).The higher efficiency of sonophotocatalytic process is due to the synergistic effect (more reactive radicals produced) [43].

In general, the nanoparticle surface generates positively charged holes (h^+) under ultrasonic irradiation, which will react with water molecules to produces more $^{\bullet}H$, $^{\bullet}OH$, $^{\bullet}HO_2$, etc. On the other hand, e^- might be involved in the generation of $O_2^{\bullet-}$ radicals by reacting with molecular oxygen (adsorbed O_2). Similarly, the reactive radicals are generated under direct photocatalytic illumination on the $MgTi_2O_5$ nanoparticle surface. Only the sonocatalytic process showed a lower catalytic activity for CV degradation (k = 0.00197 min^{-1}) due to acoustic cavitation Further, the photocatalytic process alone revealed a moderate catalytic activity (k = 0.0142 min^{-1}) for CV degradation that could be attributed to a reduction in the accessibility of surface sites for the formation of reactive radicals. The combined US irradiation and UV illumination (sonophotocatalytic process) enhanced the formation of reactive radicals and mass transfer between the bulk liquid and dispersion of $MgTi_2O_5$ nanoparticles leading to a higher degradation of CV (k = 0.0402 min^{-1}). Further, the percentage of synergy was calculated using the rate constants values using Eq. (2).

$$\text{Synergy } (\%) = \frac{k_{\text{sonophotocatalytic}} - (k_{\text{photocatalytic}} + k_{\text{sonocatalytic}})}{k_{\text{sonophotocatalytic}}} \times 100 \quad (2)$$

Therefore, the results indicate that the huge synergistic effect play under sonophotocatalytic process using $MgTi_2O_5$ nanoparticles for CV dye degradation. The enhancement of synergy during the sonophotocatalytic process was found to be about 60% when compared with the pristine photocatalytic and sonocatalytic process in the present work. In addition, the sonophotocatalytic activity for degradation of triphenylmethane dyes (cationic; BF and anionic; AF) was also studied. Fig. 5a and b show the sonophotocatalytic degradation data of these dyes (BF and AF) using $MgTi_2O_5$ nanoparticles. After 60 min, these dyes are almost completely removed. Then, the sonophotocatalytic degradation kinetic is shown in Fig. 5c and d. The results exhibit pseudo-first-order kinetic and observed rate constants (k) 0.0475 min^{-1} and 0.0277 min^{-1} for BF and AF dyes, respectively.

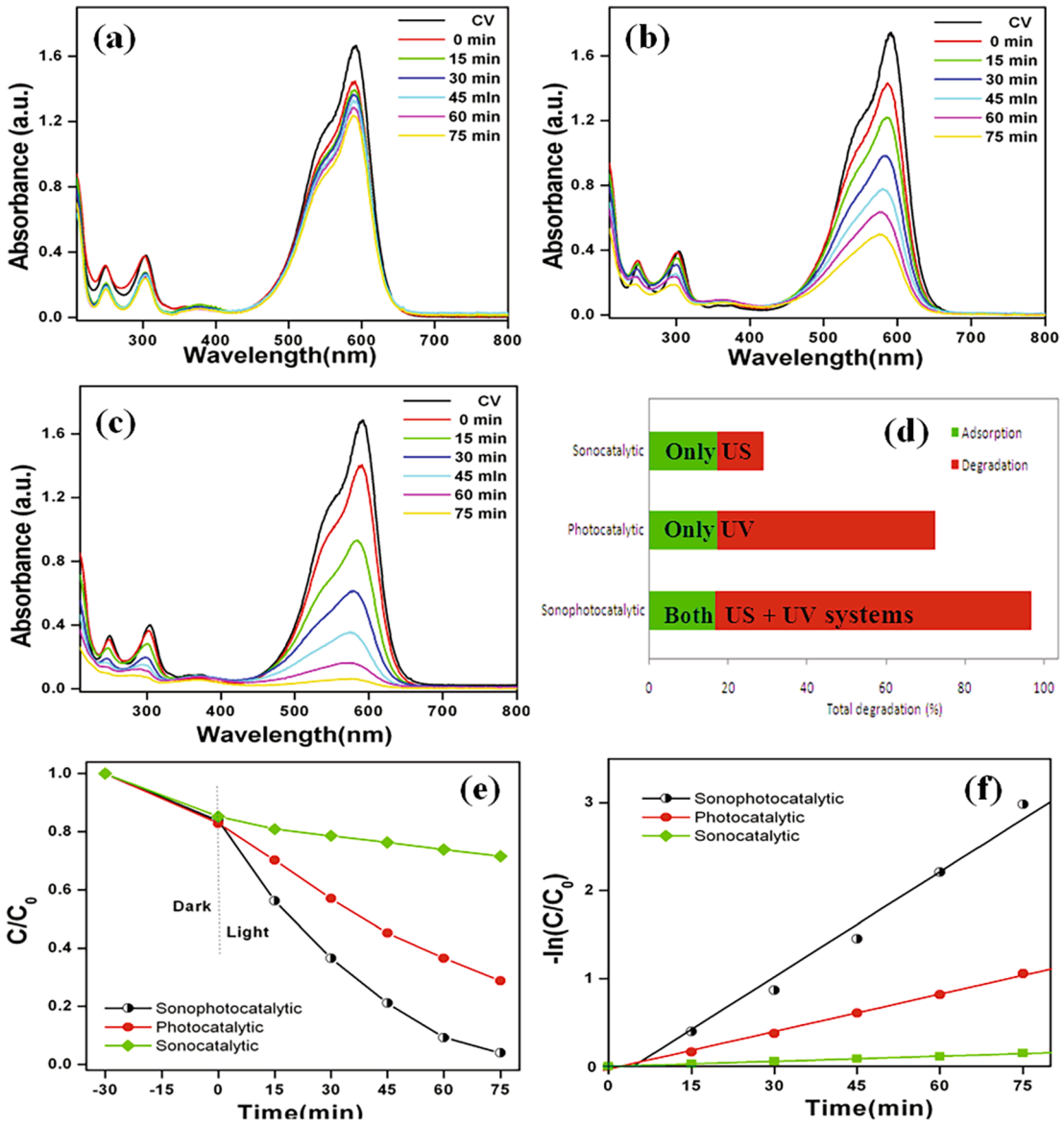

Fig 4. Time dependant UV–vis absorption spectra of (a) sonocatalytic, (b) photocatalytic, and (c) sonophotocatalytic degradation of crystal violet using $MgTi_2O_5$ nanoparticles. (d) Adsorption/degradation profile, (e) degradation curves, and (f) corresponding kinetic plots of crystal violet solution. (For interpretation of the references to colour in this figure legend, the reader is referred to the web version of this article.)

The results revealed for the cationic dye (BF) under dark adsorption was 13.5%, whereas the anionic dye (AF) showed 60% indicating that $MgTi_2O_5$ nanoparticles (Fig. 5a and b). The ζ-potential for $MgTi_2O_5$ nanoparticles was measured as a function of solution pH. Under acidic conditions, the ζ-potential was found to be positive potential. The ζ-potential decreased at alkaline pH (inset in scheme 1). The as-prepared $MgTi_2O_5$ nanoparticles have a net positive charge on the surface, which led to the strong adsorption of AF. The cationic dyes (CV and BF) were repelled from the surface $MgTi_2O_5$ nanoparticles. The degradation efficiency for triphenylmethane dyes with different catalysts or processes is compared with these results and summarized in Table 1.

To understand, the mechanism of this photocatalytic process was further investigated. The optical absorption of $MgTi_2O_5$ nanoparticles was studied (Fig. 6a) and the bandgap energy (E_g) was calculated by plotting the values of $(\alpha h\nu)^2$ *vs* the photon energy ($h\nu$) (inset Fig. 6a). The relationship between the absorption coefficient and the reflectance of the sample is calculated by the Tauc approach using Eq. (3).

$$\alpha = \frac{C\left(h\nu - E_g^{bulk}\right)^n}{h\nu} \tag{3}$$

where α is the absorption coefficient. C is a constant, $h\nu$ is the photon energy and E_g^{bulk} is the bandgap energy of the sample. The value of n is found to be dependent upon the type of transitions involved in the semiconductors (n = 2 for a direct transition and n = ½ for an indirect transition). Based on the above, the estimated value of the bandgap energy (E_g) is found to be 3.35 eV of $MgTi_2O_5$ nanoparticles for the direct transition. The observed bandgap energy of $MgTi_2O_5$ nanoparticles is almost close to the theoretical value (3.4 eV) [10]. The conduction band (E_{CB}) and the valence band (E_{VB}) positions of $MgTi_2O_5$ nanoparticles are calculated using Eqs. (4)–(5) (E_g = 3.35 eV).

$$E_{VB} = \chi - E_e + 0.5\ E_g \tag{4}$$

$$E_{CB} = E_{VB} - E_g \tag{5}$$

The absolute electronegativity (χ) of $MgTi_2O_5$ is calculated as the

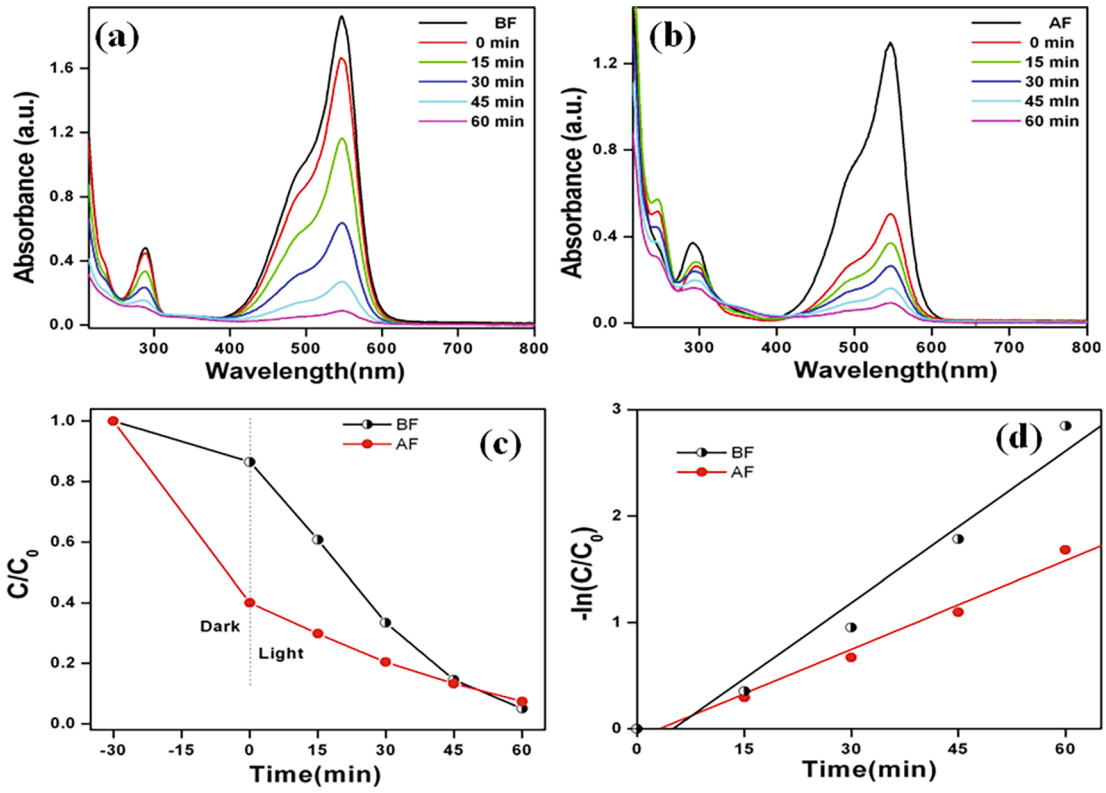

Fig 5. Time dependant UV–vis absorption spectra of (a) basic fuchsin and (b) acid fuchsin solutions during the sonophotocatalytic degradation by $MgTi_2O_5$ nanoparticles. (c) change in concentration with time curves and (d) first-order kinetic plots of corresponding samples.

geometric mean of the absolute electronegativity of constituent atoms Mg (3.75 eV), Ti (3.45 eV), and O (7.54 eV), respectively [51]. E_e is the energy of free electrons on the hydrogen scale ($E_e = 4.5$ eV). The value of χ is calculated to be 5.68 eV for $MgTi_2O_5$ and the estimated E_{VB} and E_{CB} of about 2.85 eV and −0.49 eV, respectively. The PL spectrum of $MgTi_2O_5$ nanoparticles (Fig. 6b) exhibits a strong emission band at 358 nm (excitation wavelength of 286 nm) due to the recombination of photo-generated charge carriers (electron (e) and hole (h)). In addition, the emission peaks at 397, 420, 440, 452, 470, 483, 493, and 523 nm are attributed to surface defects and trapped electrons present on the $MgTi_2O_5$ nanoparticles. Laser flash photolysis data show transient absorption signals on $MgTi_2O_5$ nanoparticles at different excitation wavelengths (Fig. 6c). The decay of transient absorption signals indicates the internal electron/hole recombination [52,53]. Further, the E_{CB} position of $MgTi_2O_5$ nanoparticles is calculated and found to be more negative than that of $O_2/O_2^{\bullet-}$ (-0.33 eV *vs.* NHE) which allows the generation of electrons for photoreduction. The generation of superoxide $O_2^{\bullet-}$ radical was analyzed with nitroblue tetrazolium as a probe molecule under UV illumination and sonochemical irradiation processes. However, the UV–vis spectrum in Fig. 7a shows a gradual decrease in nitroblue tetrazolium absorption at 259 nm during photocatalytic illumination [54]. Whereas, the pristine sonocatalytic irradiation displays a negligible amount decrease in absorption (259 nm) (Fig. 7b). This illustrates that the superoxide $O_2^{\bullet-}$ radical has been generated only under UV illumination in the presence of $MgTi_2O_5$ nanoparticles (however absolutely negligible in the sonochemical irradiation).

Then, the E_{VB} position of $MgTi_2O_5$ nanoparticles was also calculated and the value is close to that of $^{\bullet}OH/H_2O$ (2.8 eV *vs.* NHE) oxidation potential. Furthermore, the $MgTi_2O_5$ nanoparticles were tested for $^{\bullet}OH$ radical generation by PL studies with terephthalic acid as a probe molecule (photooxidation through-hole) [55]. The PL spectrum shows that the emission peak at 425 nm gradually increases due to the formation of 2-hydroxy terephthalic acid via $^{\bullet}OH$ radical oxidation (photocatalytic illumination) (Fig. 7c). Besides, the ultrasonic irradiation was also tested for the production of reactive radicals using terephthalic acid probe molecule ($^{\bullet}OH$ radical generation) [56]. In this case, the PL results indicate that $^{\bullet}OH$ radicals were generated during ultrasonic irradiation using $MgTi_2O_5$ nanoparticles (relatively one-half of photocatalytic illumination) (Fig. 7d). Hence, under the sonophotocatalytic processes both superoxide $O_2^{\bullet-}$ radical and $^{\bullet}OH$ radical generation takes place which results in enhanced degradation of triphenylmethane dyes (CV, BF, and AF) over$MgTi_2O_5$ nanoparticles as shown in Eqs. (6)–(11). Based on the above discussion, a mechanism for the sonophotocatalytic degradation of triphenylmethane dyes is proposed as depicted in Scheme 2.

$$MgTi_2O_5 + h\nu \rightarrow MgTi_2O_5\,(e^-_{CB}) + MgTi_2O_5(h^+_{VB}) \quad (6)$$

$$MgTi_2O_5 +)))) \rightarrow MgTi_2O_5\,(e^-_{CB}) + MgTi_2O_5(h^+_{VB}) \quad (7)$$

$$MgTi_2O_5\,(e^-_{CB}) + O_2 \rightarrow MgTi_2O_5 + O_2^{\bullet-} \quad (8)$$

$$MgTi_2O_5(h^+_{VB}) + H_2O \rightarrow {}^{\bullet}OH + H^+ + MgTi_2O_5 \quad (9)$$

$$4H_2O +)))) \rightarrow 5{}^{\bullet}H + 2{}^{\bullet}OH + {}^{\bullet}HO_2 \quad (10)$$

$${}^{\bullet}OH + {}^{\bullet}H + {}^{\bullet}HO_2 + O_2{}^{\bullet-} + \text{Triphenylmethanedyes} + h\nu +)))) \rightarrow \text{Degradation products} \quad (11)$$

4. Conclusions

In conclusion, phase pure $MgTi_2O_5$ catalytic nanoparticles were synthesized by a simple hydrothermal post-annealing method. The morphological features confirm that a large number of $MgTi_2O_5$ nanoparticles aggregate into honeycomb-like structures.The $MgTi_2O_5$ nanoparticles are crystalline in-nature containing defects with trapped electrons on the surface. The optical bandgap energy of as-prepared

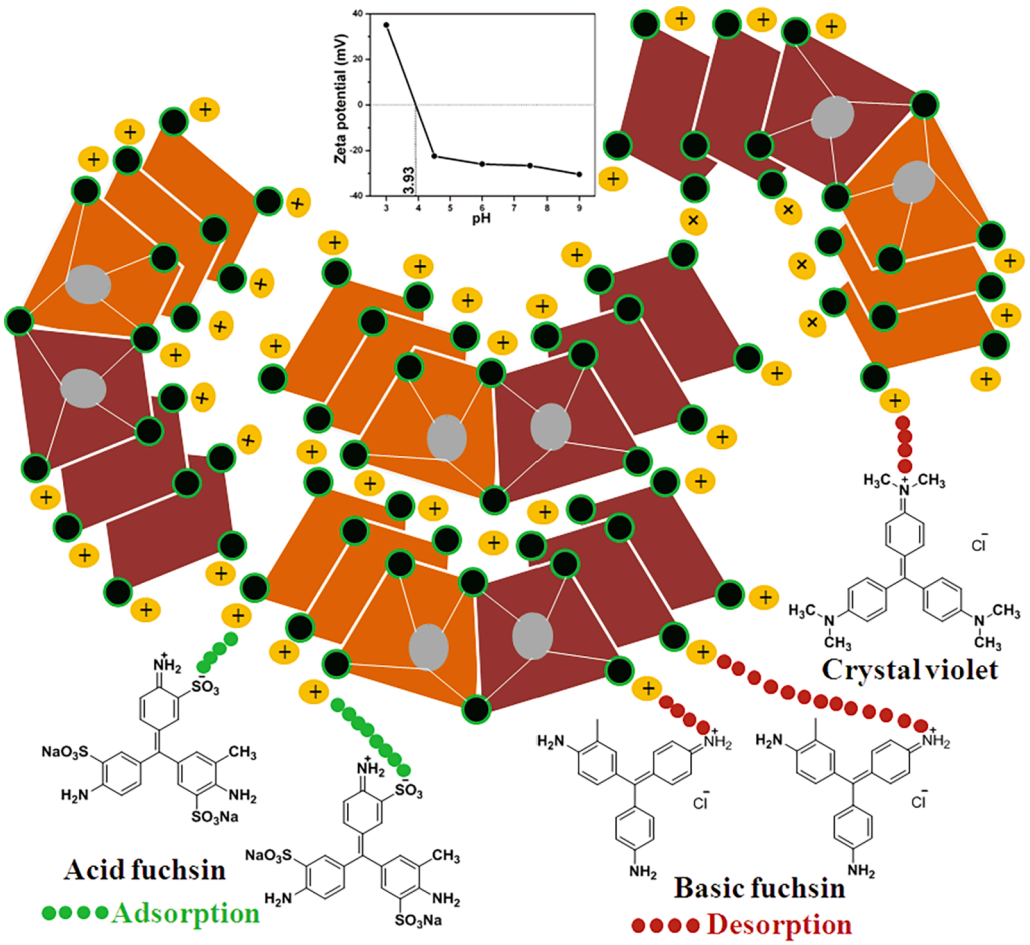

Scheme 1. The schematic diagram for adsorption and desorption of triphenylmethane dyes with $MgTi_2O_5$ nanoparticles (inset shows the ζ-potential data).

Table 1
Degradation efficacy of triphenylmethane dyes with different catalysts.

Catalyst	Irradiation source	Concentration of catalyst	Concentration of dyes	Degradation efficacy	Reference
Nanocrystalline Bi_2WO_6	20 W (UV-365 nm lamps)	0.05 g L^{-1}	100 mL of CV (50 ppm)	80.1% at 24 h	[44]
$Ga_2Zr_{2-x}W_xO_7$	82 lm W^{-1} (visible metal halide lamp)	1 g L^{-1}	4 mg L^{-1} of CV	Disappears after 360 min	[45]
Mesoporous titania	Two 20 W UV lamps	0.5 g L^{-1}	50 mL of BF (10 ppm)	69.4% at 8 h	[46]
–	Ultrasonic frequency (25 kHz; 500 W)	–	10 μmol L^{-1} of BF	75% at 60 min	[47]
ZnS nanoparticles	250 W Infrared light lamp	10 mg	20 mL of AF (1×10^{-5} mol L^{-1})	Disappears after 30 min	[48]
Zn doped SnO_2	500 W Hg lamp	0.1 g L^{-1}	4 mg L^{-1} of AF	96% at 80 min	[49]
$CuFe_2O_4$ nanotubes	175 W tungsten lamp	30 mg	50 mL of AF (15 mg L^{-1})	Disappears after 90 min	[50]
$MgTi_2O_5$ nanoparticles	100 W power (38 kHz frequency) and 6 W UV lamp	50 mg	100 mL of CV, BF, AF (5×10^{-5} mol L^{-1})	Disappears after 75 min in CV and 60 min in BF and AF	This work

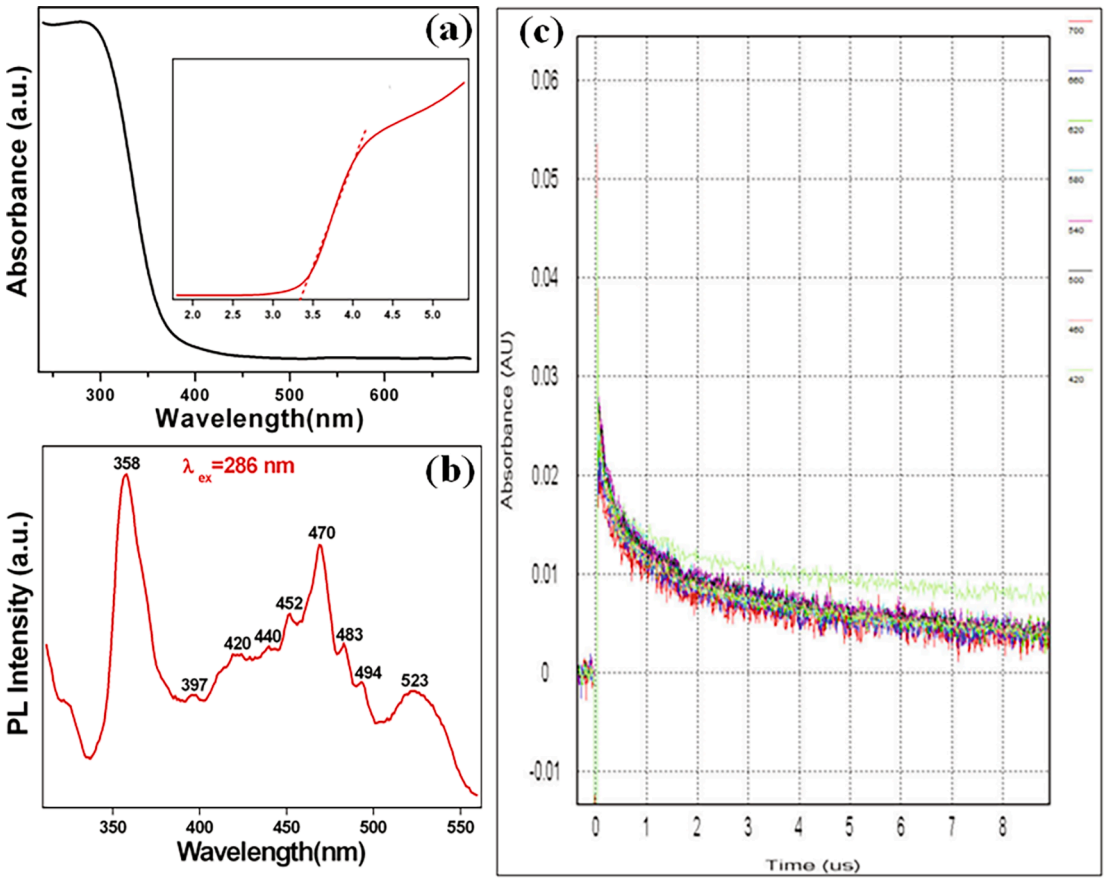

Fig 6. (a) UV–vis absorption spectrum (inset Tauc plot), (b) PL emission spectrum, and (c) Transient absorption *vs.* time curve of $MgTi_2O_5$ nanoparticles at different excitation wavelengths.

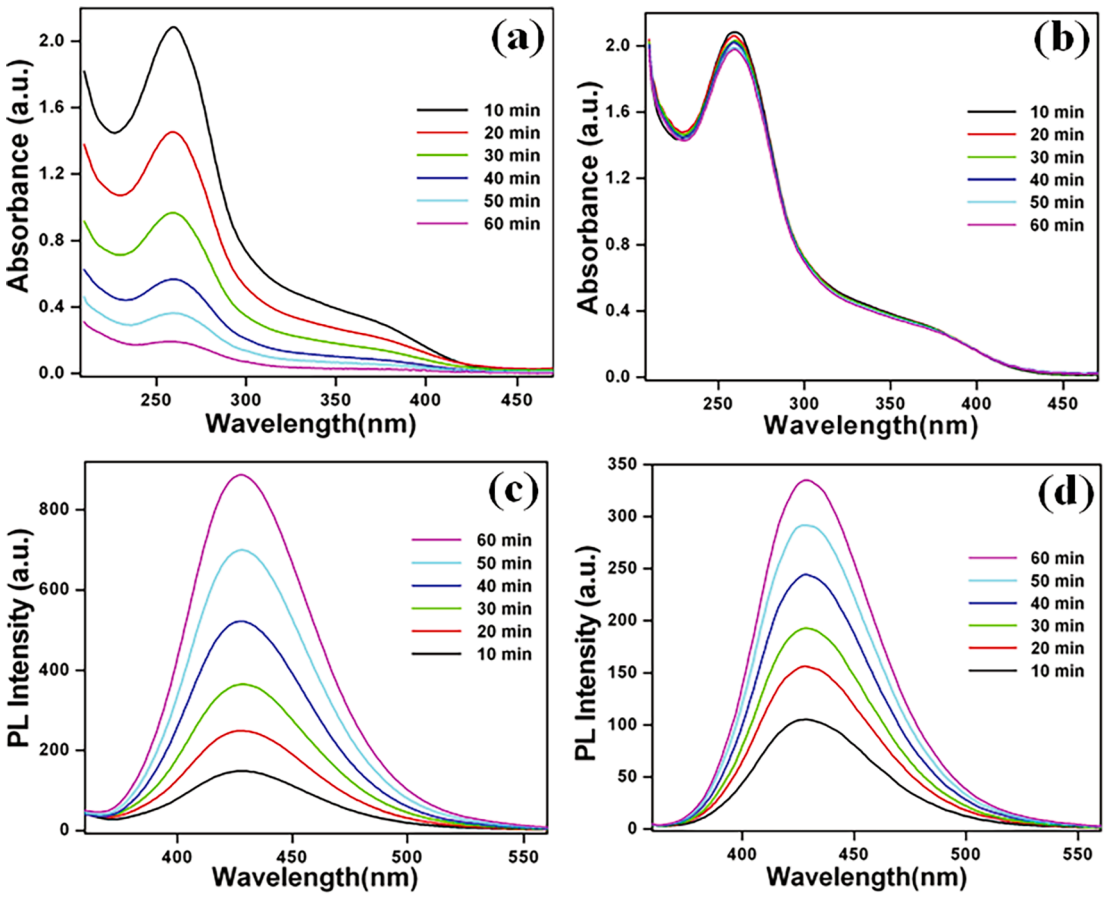

Fig 7. UV-vis absorption spectra of nitroblue tetrazolium solution (a) photocatalytic illumination and (b) sonocatalytic irradiation using $MgTi_2O_5$ nanoparticles; PL emission spectra of terephthalic acid in alkaline solution under (c) photocatalytic illumination and (d) sonocatalytic irradiation with$MgTi_2O_5$ nanoparticles.

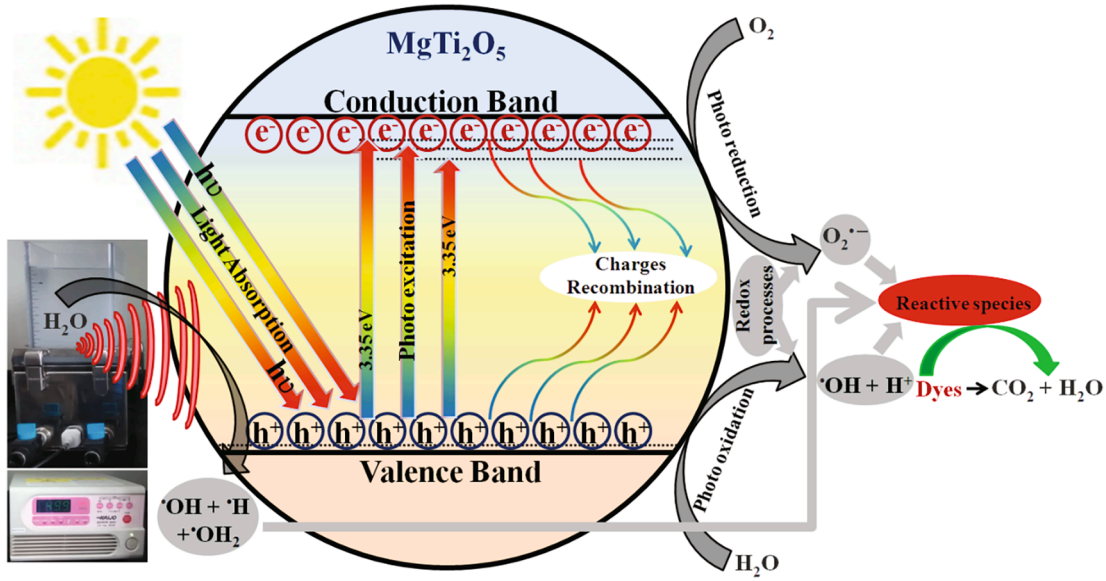

Scheme 2. Schematic illustration of sonophotocatalytic degradation for triphenylmethane dyes over $MgTi_2O_5$ nanoparticles.

$MgTi_2O_5$ nanoparticles was found to be 3.35 eV for the direct transition. The sonophotocatalytic activity towards the degradation of crystal violet revealed a strong synergetic effect compared to that of photocatalytic and sonocatalytic processes. In addition, the basic fuchsin and acid fuchsin were completed degraded by the sonophotocatalytic process within 60 min using $MgTi_2O_5$ nanoparticles as a catalyst. The as-prepared $MgTi_2O_5$ nanoparticles can be used as a sonophotocatalyst for environmental remediation processes such as waste-water treatment.

Declaration of Competing Interest

The authors declare that they have no known competing financial interests or personal relationships that could have appeared to influence the work reported in this paper.

Acknowledgment

The Department of Science and Technology, India sponsored this research under the Nanomission scheme (SR/NM/NS-1024/2016). Authors MA and SA thank SPARC (MHRD, INDIA) for the joint project.

References

[1] K. Mageshwari, S.S. Mali, R. Sathyamoorthy, P.S. Patil, Template-free synthesis of MgO nanoparticles for effective photocatalytic applications, Powder Technol. 249 (2013) 456–462.
[2] M.M.M.G. Prasangagayanathmantilaka, R.T. De Silva, S.P. Ratnayake, G. Amaratunga, K.M. Nalin de Silva, Photocatalytic activity of electrospun MgO nanofibres: synthesis, characterization and applications, Mater. Res. Bull. 99 (2018) 204–210.
[3] T. Selvamani, A. Sinhamahapatra, D. Bhattacharjya, I. Mukhopadhyay, Rectangular MgO microsheets with strong catalytic activity, Mater. Chem. Phys. 129 (3) (2011) 853–861.
[4] J. Bandara, C.C. Hadapangoda, W.G. Jayasekera, TiO_2/MgO composite photocatalyst: the role of MgO in photoinduced charge carrier separation, Appl. Catal. B Environ. 50 (2004) 83–88.
[5] D. Arikal, A. Kallingal, Photocatalytic degradation of azo and anthraquinone dye using TiO2/MgO nanocomposite immobilized chitosan hydrogels, Environ. Technol. https://doi.org/10.1080/09593330.2019.1701094.
[6] G. Zheng, J. Wang, X. Liu, A. Yang, H. Song, Y. Guo, H. Wei, C. Jiao, S. Yang, Q. Zhu, Z. Wang, Valence band offset of MgO/TiO_2 (rutile) heterojunction measured by X-ray photoelectron spectroscopy, Appl. Surf. Sci. 256 (23) (2010) 7327–7330.
[7] U.O. Bhagwat, J.J. Wu, A.M. Asiri, S. Anandan, Synthesis of $MgTiO_3$ Nanoparticles for photocatalytic applications, ChemistrySelect. 4 (2019) 788–796.
[8] M.M. Medić, M. Vasić, A.R. Zarubica, L.V. Trandafilović, G. Dražić, M. D. Dramićanin, J.M. Nedeljković, Enhanced photoredox chemistry in surface-modified Mg_2TiO_4nano-powders with bidentate benzene derivatives, RSC Adv. 6 (97) (2016) 94780–94786.
[9] M.A. Ehsan, R. Naeem, V. McKee, A.S. Hakeem, M. Mazhar, $MgTi_2O_5$ thin films from single molecular precursor for photoelectrochemical water splitting, Sol. Energy Mater. Sol. Cells. 161 (2017) 328–337.
[10] N. Zhang, K. Zhang, W. Zhou, B. Jiang, K. Pan, Y. Qu, G. Wang, Pure phase orthorhombic $MgTi_2O_5$ photocatalyst for H_2 production, RSC Adv. 5 (128) (2015) 106151–106155.
[11] Y. Suzuki, Y. Shinoda, Magnesium dititanate ($MgTi_2O_5$) with pseudobrookite structure: a review, Sci. Technol. Adv. Mater. 12 (3) (2011) 034301, https://doi.org/10.1088/1468-6996/12/3/034301.
[12] X. Wang, J. Cai, Y. Zhang, L. Li, L.i. Jiang, C. Wang, Heavy metal sorption properties of magnesium titanate mesoporous nanorods, J. Mater. Chem. A. 3 (22) (2015) 11796–11800.
[13] Y. Nakagoshia, Y. Suzukia, Pseudobrookite-type $MgTi_2O_5$ water purification filter with controlled particle morphology, J. Asian, Ceram. Soc. 3 (2015) 334–338.
[14] F. Xie, Y. Deng, Y. Xie, H. Xu, G. Chen, Ultra-small nanoparticles of $MgTi_2O_5$ embedded in carbon rods with superior rate performance for sodium ion batteries, Chem. Commun. 51 (17) (2015) 3545–3548.
[15] Y. Qu, W. Zhou, Y. Xie, L. Jiang, J. Wang, G. Tian, Z. Ren, C. Tian, H. Fu, A novel phase-mixed $MgTiO_3$–$MgTi_2O_5$ heterogeneous nanorod for high efficiency photocatalytic hydrogen production, Chem. Commun. 49 (76) (2013) 8510, https://doi.org/10.1039/c3cc43435d.
[16] S. Singh, V.C. Srivastava, I.D. Mall, Mechanism of dye degradation during electrochemical treatment, J. Phys. Chem. C. 117 (29) (2013) 15229–15240.
[17] N. López-Gutiérrez, R. Romero-González, J.L.M. Vidal, A.G. Frenich, Analysis of triphenylmethane dyes in seafood products:a review of extraction methods and determination by liquid chromatography coupled to mass spectrometry, Anal. Methods. 5 (2013) 3434–3449.
[18] F. Kazemi, Z. Mohamadnia, B. Kaboudin, Z. Karimi, Photodegradation of methylene blue with a titanium dioxide/polyacrylamide photocatalyst under sunlight, J. Appl. Polym. Sci. 133 (2016) 1.
[19] Y. Zou, X. Wang, A. Khan, P. Wang, Y. Liu, A. Alsaedi, T. Hayat, X. Wang, Environmental remediation and application of nanoscale zero-valent iron and its composites for the removal of heavy metal ions, Environ. Sci. Technol. 50 (2016) 7290–7304.
[20] K.G. Bhattacharyya, A. Sarma, Adsorption characteristics of the dye, brilliant green, on neem leaf powder, Dyes Pigm. 57 (2003) 211–222.
[21] M.N.V.R. Kumar, T.R. Sridhari, K.D. Bhavani, P.K. Dutt, Trends in color removal from textile mill effluents, Colorage 40 (1998) 25–34.
[22] S.H.S. Chan, T.Y. Yeong Wu, J.C. Juan, C.Y. Teh, Recent developments of metal oxide semiconductors as photocatalysts in advanced oxidation processes (AOPs) for treatment of dye waste-water, J. Chem. Technol. Biotechnol. 86 (9) (2011) 1130–1158.
[23] M. Pirsaheb, N. Moradi, Sonochemical degradation of pesticides in aqueous solution: investigation on the influence of operating parameters and degradation pathway-a systematic review, RSC Adv. 10 (2020) 7396–7423.
[24] C.G. Joseph, G.L. Puma, A. Bono, D. Krishnaiah, Sonophotocatalysis in advanced oxidation process: a short review, Ultrason. Sonochem. 16 (5) (2009) 583–589.
[25] K.P. Jyothi, S. Yesodharan, E.P. Yesodharan, Contaminant salts as enhancers of sonocatalytic degradation of organic water pollutants: effect of concentration, reaction time and adsorption on the efficiency of enhancement and the fate of concurrently formed H_2O_2, J. Environ. Chem. Engg. 6 (2018) 3574–3589.
[26] G.K. Dinesh, S. Anandan, T. Sivasankar, Sonophotocatalytic treatment of bismarck brown G dye and real textile effluent using synthesized novel Fe(0)-doped TiO_2 catalyst, RSC Adv. 5 (14) (2015) 10440–10451.
[27] S. Anandan, N. Pugazhenthiran, T. Selvamani, S.-H. Hsieh, G.-J. Lee, J.J. Wu, Investigation on photocatalytic potential of Au-Ta_2O_5 semiconductor nanoparticle by degrading methyl orange in aqueous solution by illuminating with visible light, Catal. Sci. Technol. 2 (12) (2012) 2502, https://doi.org/10.1039/c2cy20393f.
[28] S. Anandan, G.-J. Lee, P.-K. Chen, C. Fan, J.J. Wu, Removal of orange II dye in water by visible light assisted photocatalytic ozonation using Bi_2O_3 and Au/Bi_2O_3 nanorods, Ind. Eng. Chem. Res. 49 (20) (2010) 9729–9737.
[29] F. Ghanbari, M. Moradi, Application of peroxymonosulfate and its activation methods for degradation of environmental organic pollutants: review, Chem. Eng. J. 310 (2017) 41–62.
[30] T. Selvamani, C.A. Manjula, S. Anandan, A.M. Asiri, M. Ashokkumar, Preparation of CuOmesocrystals via antlerite intermediate for photocatalytic applications, Cryst. Res. Technol. 50 (2) (2015) 143–149.
[31] X. Lin, M. Sun, B. Gao, W. Ding, Z. Zhang, S. Anandan, A. Umar, Hydrothermally regulating phase composition of TiO_2 nanocrystals toward high photocatalytic activity, J. Alloys. Compd. 850 (2021), 156653.
[32] B. Gao, M. Sun, W. Ding, Z. Ding, W. Liu, Decoration of γ-graphyne on TiO_2 nanotube arrays: improved photoelectrochemical and photocatalytic properties, Appl. Catal. B Environ. 281 (2021), 119492.
[33] W. Ding, M. Sun, Z. Zhang, X. Lin, B. Gao, Ultrasound-promoted synthesis of γ-graphyne for supercapacitor and photoelectrochemical applications, Ultrason. Sonochem. 61 (2020), 104850.
[34] M. Sun, Y. Yao, W. Ding, S. Anandan, N/Ti^{3+} co-doping biphasic TiO_2/Bi_2WO_6 heterojunctions: hydrothermal fabrication and sonophotocatalytic degradation of organic pollutants, J. Alloys. Compd. 820 (2020), 153172.
[35] M. Zargazi, M.H. Entezari, Sonochemical versus hydrothermal synthesis of bismuth tungstate nanostructures: photocatalytic, sonocatalytic and sonophotocatalytic activities, Ultrason. Sonochem. 51 (2019) 1–11.
[36] A. Khataee, T.S. Rad, S. Nikzat, A. Hassani, M.H. Aslan, M. Kobya, E. Demirbaş, Fabrication of NiFe layered double hydroxide/reduced graphene oxide (NiFe-LDH/rGO) nanocomposite with enhanced sonophotocatalytic activity for the degradation of moxifloxacin, Chem. Eng. J. 375 (2019), 122102.
[37] A. Manivel, S. Naveenraj, P.S. Sathish Kumar, S. Anandan, CuO-TiO_2 nanocatalyst for photodegradation of acid red 88 in aqueous solution, Sci. Adv. Mater. 2 (1) (2010) 51–57.
[38] M. He, B. Winkler, J.D. Bauer, L. Bayarjargal, J. Ruiz-Fuertes, I. Alencar, W. Morgenroth, K. Refson, V. Milman, Lattice dynamics and Mg/Ti order in orthorhombic pseudobrookite-type $MgTi_2O_5$, J. Alloys. Compd. 699 (2017) 16–24.
[39] H. Liermann, R.T. Downs, H. Yang, Site disorder revealed through Raman spectra from oriented single crystals:a case study on karooite ($MgTi_2O_5$), American Mineralogist. 91 (2006) 790–793.
[40] J. Shen, Y. Li, H. Zhao, K. Pan, X. Li, Y. Qu, G. Wang, D. Wang, Modulating the photoelectrons of g-C_3N_4 via coupling $MgTi_2O_5$ as appropriate platform for visible-light-driven photocatalytic solar energy conversion, Nano Res. 12 (8) (2019) 1931–1936.
[41] N. Zhang, Y. Qu, K. Pan, G. Wang, Y. Li, Synthesis of pure phase $Mg_{1.2}Ti_{1.8}O_5$ and $MgTiO_3$ nanocrystals for photocatalytic hydrogen production, Nano Res. 9 (3) (2016) 726–734.
[42] H.-Y. Jiang, P. Li, G. liu, J. Ye, J. Lin, Synthesis and photocatalytic properties of metastable β-Bi_2O_3 stabilized by surfacecoordination effects, J. Mater. Chem. A. 3 (9) (2015) 5119–5125.
[43] G. Eshaq, A.E. ElMetwally, Bmim[OAc]-Cu_2O/g-C_3N_4 as a multi-function catalyst for sonophotocatalytic degradation of methylene blue, Ultrason. Sonochem. 53 (2019) 99–109.
[44] Y.-H. Liao, J.X. Wang, J.-S. Lin, W.-H. Chung, W.-Y. Lin, C.-C. Chen, Synthesis, photocatalytic activities and degradation mechanism of Bi_2WO_6 toward crystal violet dye, Catal. Today 174 (1) (2011) 148–159.
[45] H.A. Abbas, R.A. Nasr, R. Abu-Zurayk, A. Al Bawab, T.S. Jamil, Decolourization of crystal violet using nano-sized novel fluorite structure $Ga_2Zr_{2-x}W_xO_7$ photocatalyst undervisible light irradiation, R. Soc. Open. Sci 7 (3) (2020) 191632, https://doi.org/10.1098/rsos.191632.
[46] J. Tao, W. Gong, Z. Yan, D. Duan, Y. Zeng, J. Wang, UV/visible-light photodegradation of organic dyes over mesoporous titania prepared by using 2,4,5-triphenylimidazole as template, Mater. Sci. Semicond. Process. 27 (2014) 452–460.
[47] R-J. Lan, T-J. Li, B. H. Chen, Ultrasonic degradation of fuchsin basic in aqueous solution: effects of operating parameters and additives, Inter. J. Photoenergy. 2013, Artile ID: 893131, https://doi.org/10.1155/2013/893131.
[48] S. Xiong, B. Xi, C. Wang, D. Xu, X. Feng, Z. Zhu, Y. Qian, Tunable synthesis of various Wurtzite ZnS architectural structures and their photocatalytic properties, Adv. Funct. Mater. 17 (15) (2007) 2728–2738.
[49] H. Huang, S. Tian, J. Xu, Z. Xie, D. Zeng, D. Chen, G. Shen, Needle-like Zn-doped SnO_2 nanorods with enhanced photocatalytic and gas sensing properties, Nanotechnology 23 (2012), 105502.

[50] P. Jing, J. Li, L. Pan, J. Wang, X. Sun, Q. Liu, Efficient photocatalytic degradation of acid fuchsin in aqueous solution using separate porous tetragonal-$CuFe_2O_4$ nanotubes, J. Hazard. Mater. 284 (2015) 163–170.
[51] R.G. Pearson, Absolute electronegativity and hardness: application to inorganic chemistry, Inorg. Chem. 27 (1988) 734–740.
[52] S.G. Ullattil, P. Periyat, B. Naufal, M.A. Lazar, Self-doped ZnO microrods-high temperature stable oxygen deficient platforms for solar photocatalysis, Ind. Eng. Chem. Res. 55 (22) (2016) 6413–6421.
[53] J. Nie, J. Schneider, F. Sieland, L. Zhou, S. Xia, D.W. Bahnemann, New insights into the surface plasmon resonance (SPR) driven photocatalytic H_2 production of Au-TiO_2, RSC Adv. 8 (46) (2018) 25881–25887.
[54] V.L. Prasanna, V. Rajagopalan, A new synergetic nanocomposite for dye degradation in dark and light, Sci. Rep. 6 (2016) 38606.
[55] T. Selvamani, S. Anandan, L. Granone, D.W. Bahnemann, M. Ashokkumar, Phase-controlled synthesis of bismuth oxide polymorphs for photocatalytic applications, Mater. Chem. Front. 2 (9) (2018) 1664–1673.
[56] D.B. Rajamma, S. Anandan, N.S.M. Yusof, B.G. Pollet, M. Ashokkumar, Sonochemical dosimetry: a comparative study of Weissler, Fricke and terephthalic acid methods, Ultrason. Sonochem. 72 (2021), 105413.